International Journal of Solids and Structures 50 (2013) 4241–4257

Contents lists available at ScienceDirect

International Journal of Solids and Structures

journal homepage: www.elsevier.com/locate/ijsolstr

Tension–torsion fracture experiments—Part I: Experiments and a procedure to evaluate the equivalent plastic strain

Jonas Faleskog [a,*], Imad Barsoum [b]

[a] Department of Solid Mechanics, Royal Institute of Technology, SE-100 44 Stockholm, Sweden
[b] Department of Mechanical Engineering, The Petroleum Institute, P.O. Box 2533, Abu Dhabi, United Arab Emirates

ARTICLE INFO

Article history:
Available online 4 September 2013

Keywords:
Ductile fracture
Fracture in shear
Tension–torsion test
Lode parameter

ABSTRACT

Ductile failure experiments on a double notched tube (DNT) specimen subjected to a combination of tensile load and torque that was applied at a fixed ratio is presented. The experimental results extend those in Barsoum and Faleskog (2007a) down to zero stress triaxiality. A new and robust evaluation procedure for such tests is proposed, and a simple relation for the equivalent plastic strain at failure for combined normal and shear deformation, respectively, is developed. Tests were carried out on the medium strength medium hardening steel Weldox 420, and the high strength low hardening steel Weldox 960. The experimental results unanimously show that ductile failure not only depends on stress triaxiality, but is also strongly affected by the type of deviatoric stress state that prevails, which can be quantified by a stress invariant that discriminates between axisymmetric stressing and shear dominated stressing, e.g., the Lode parameter. Additional experiments on round notch bar (RNB) specimens are recapitulated in order to give a comprehensive account on how ductile failure depends on stress triaxiality, ranging from zero to more than 1.6, and the type of stress state for the two materials tested. This provides an extensive experimental data base that will be used to explore an extension of the Gurson model that incorporates damage development in shear presented in Xue et al. (2013) (Part II).

1. Introduction

There is now a convincing amount of experimental data showing that ductile fracture is affected not only by stress triaxiality, but also depends on the deviatoric stress state in some metallic alloys. This is especially noticeable in the lower stress triaxiality regime as demonstrated in tests on Al 2024-T351 by Bao and Wierzbicki (2004), and for two different steels by Barsoum and Faleskog (2007a) in experiments on a double notched tube (DNT) specimen subjected to combined tension–torsion load. These experiments unanimously show in a systematic way that ductile fracture is not necessary monotonically related to stress triaxiality. Indications of this behavior was noted already by McClintock (1971), who in primarily high strength low hardening steels obtained a lower ductility in pure torsion tests than in tension tests with significantly higher triaxiality. Further support of this non-monotonic behavior can be found in recent experimental studies. For instance, Mohr and co-worker develop a new specimen and test set-up for applying a combination of tensile and shear load on sheet metals (Mohr and Henn, 2007). In a series of tests on a TRIP780 steel, they observe a similar fracture trend as discussed above (Dunand and Mohr, 2011). Gruben et al. (2011) investigate a cold-rolled dual-phase steel sheet by use of five different experimental set-ups, and find a moderate variation of ductility in the limited range of stress states available from their test. By testing axisymmetric and plane strain specimens, Gao and co-workers observe that ductility in a DH36 steel is strongly affected by the deviatoric stress state (Gao et al., 2010), whereas this is not the case in Aluminum 5083 (Gao et al., 2009). They also examine a different type of tube specimen with a more smooth test section that allows for a more direct estimate of the stress and strain state during a test, but where the essentially plane stress conditions that prevails in the test section limits the maximum achievable stress triaxiality to about 0.57 (Graham et al., 2012). Very recently, yet another tube geometry with a smooth test section is proposed by Haltom et al. (2013), who carry out tension–torsion tests on Al-6061-T1 seamless drawn tubes. Their experiments involved radial paths of relatively high shear and axial stress. In the regime considered the failure strain increased monotonically as the triaxiality decreased.

A common feature of ductile fracture in the above experimental results is that the sensitivity to the deviatoric stress state tends to increase as stress triaxiality decrease towards zero. The underlying reason for this behavior can in part be explained by a change in fracture mechanism to a mode where rotation and collapse of voids driven by intense shearing leads to severe material softening and

* Corresponding author.
E-mail address: faleskog@kth.se (J. Faleskog).

0020-7683/$ - see front matter © 2013 Elsevier Ltd. All rights reserved.
http://dx.doi.org/10.1016/j.ijsolstr.2013.08.029

failure. This change in mechanism is explored in a series of micromechanical studies by Barsoum and Faleskog (2007b, 2011) and Tvergaard (2008, 2009). To bridge the gap to existing continuum damage constitutive models, Nahshon and Hutchinson (2008) propose an extension to the Gurson model that addresses this failure mechanism in a phenomenological way. So far, the predictive capability of the extended Gurson model has been confirmed in a micromechanical study by Tvergaard and Nielsen (2010) and to some extent experimentally in Xue et al. (2010). The objective of the present paper is to significantly extend the experimental work initiated in Barsoum and Faleskog (2007a) with new tests on the DNT specimen, to cover the full range down to zero triaxiality. And, to provide a discriminating experimental basis to be utilized in full 3D simulations with the extended Gurson model, which is presented in the companion paper: Xue et al. (2013). The present paper will be designated as Part I and the companion paper as Part II. Moreover, tests on the two steels in question, i.e., Weldox 420 and Weldox 960, carried out on round notched bar (RNB) specimens (Barsoum et al., 2012) will be briefly summarized here to give a collective and self-contained experimental background to Part II.

The deviatoric stress state can for nominally isotropic materials, as will be further elaborated on in Part II, be disassembled into the extremes of two axisymmetric states with a shearing state in between, and quantified by the Lode parameter commonly defined as

$$L = \frac{2\sigma_{II} - \sigma_I - \sigma_{III}}{\sigma_I - \sigma_{III}}. \tag{1}$$

Here, $\sigma_I \geqslant \sigma_{II} \geqslant \sigma_{III}$ denote the ordered principal stresses. Hence, the Lode parameter will be limited to the interval $-1 \leqslant L \leqslant 1$, where $L = -1$ corresponds to an axisymmetric state with $\sigma_I \geqslant \sigma_{II} = \sigma_{III}$, $L = 0$ to a shearing state and $L = 1$ to an axisymmetric state with $\sigma_I = \sigma_{II} \geqslant \sigma_{III}$. Stress triaxiality is defined in the standard way as $T = \sigma_m/\sigma_e$, with σ_m being the mean stress and σ_e the von Mises effective stress. Related to the double notched tube specimen, stress states in the range $-1 \leqslant L \leqslant 0$ with T varying from zero to larger than unity can be accomplished by varying the applied combination of tension–torsion load.

As an alternative measure of the deviatoric stress state, Nahshon and Hutchinson (2008) introduce

$$\omega = 1 - \left(\frac{27J_3}{2\sigma_e^3}\right)^2 \quad \text{with } J_3 = (\sigma_I - \sigma_m)(\sigma_{II} - \sigma_m)(\sigma_{III} - \sigma_m), \tag{2}$$

to distinguish between the axisymmetric stress states ($\omega = 0$) and the shearing stress state ($\omega = 1$), where the parameter ω is limited to the interval $0 \leqslant \omega \leqslant 1$.

The plan of Part I is as follows. In Section 2, the test program is briefly summarized to give a self-contained background for the simulations with the extended Gurson model that commence in Part II. A new and robust evaluation procedure for the DNT experiments is laid out in Section 3, where also a new simplified relation is proposed for the estimation of the equivalent plastic strain under near proportional deformation paths of combined stretching and shearing. In addition, an approximate stress analysis of the DNT tests is presented that will be further elaborated on in Part II. In Section 4 the experimental results are presented and discussed, and finally the paper is concluded in Section 5.

2. Test program

A brief summary will be given here on the materials and the specimens tested. A more comprehensive description can be found in Barsoum and Faleskog (2007a) and Barsoum et al. (2012). Also, focus will be on the new tests and new evaluation procedures proposed, which are described in more detail in Section 3.

2.1. Materials

A hot rolled medium strength steel, Weldox 420, and a quenched and tempered high strength steel, Weldox 960, were investigated in the test program. Weldox 420 has a somewhat banded ferrite/pearlite microstructure, and is a medium strength and hardening material with a rather high ductility. Digital image analysis of polished and etched surfaces revealed an average grain size of 11.5 μm with a standard deviation of 4.6 μm. Weldox 960 has a martensitic microstructure and is a high strength material with a relatively low hardening. No attempt was made to measure the grain size in this heat-treated steel. However, the average size of the parent austenite grains that were formed during the high temperature hold during the heat treatment was estimated to be about 10 μm (sometimes referred to as "prior-austenite grain size") (Narström, 2013).

Both materials were delivered in plates with a thickness of 30 mm. All specimens in the experimental program were manufactured such that the tensile axis of loading was oriented in the rolling direction (L) of the plate. Uniaxial stress–strain data was determined for both materials from tests on smooth round bar specimens. The uniaxial test data from both materials was very well described by a uniaxial stress–strain on the form

$$\sigma = \begin{cases} E\varepsilon & \varepsilon \leqslant \varepsilon_0 \\ \sigma_0 & \varepsilon_0 < \varepsilon \leqslant \varepsilon_N + \varepsilon_s \\ \sigma_0((\varepsilon - \varepsilon_s)/\varepsilon_N)^N & \varepsilon > \varepsilon_N + \varepsilon_s \end{cases} \tag{3}$$

Here, σ_0 represents the initial yield stress, ε_s an offset strain, ε_N a normalizing strain and $\varepsilon_0 = \sigma_0/E$. For both materials Young's modulus E and Poisson's ratio ν were about 208 GPa and 0.3, respectively. All the material parameters in Eq. (3) are listed in Table 1 with some additional material parameters, where $R_{p0.2}$ is the 0.2% offset yield strength, R_m is the ultimate tensile strength and $\bar{\varepsilon}_f^p$ is the effective plastic strain at failure averaged over the cross section of the neck, as estimated in the standard way from uniaxial tests (neglecting elastic strains) by $2\ln(d_0/d_f)$, with d_0 and d_f referring to the diameters prior to and after the test, respectively.

In the analysis to be presented here as well as in Part II, both materials were assumed to be isotropic. To check this assumption, three-point-bend tests on uniform prismatic bar specimens with rectangular cross-sections were performed in three different directions for each material. Specifically, tests were carried out in the rolling direction (L), transverse to the rolling direction (T), and short transverse to the rolling direction (S), i.e., the thickness direction. Two tests were done in every direction. Details of these tests are described in Appendix A, where we also show that a relative difference in load ratio between two tests, directly correlate to a relative difference in flow stress. The load–deflection curves from the three-point-bend tests are shown in Fig. 1 for Weldox 420 in (a) and Weldox 960 in (b). As a small variation in the dimensions of the cross-section of the bar may have a strong influence on results, a normalized load $\overline{P}$ was introduced as described in Appendix A to eliminate this influence. In the expression for $\overline{P}$, σ_0 was taken as the material specific value as listed in Table 1, b and h are the values measured for each bend specimen as listed in Table A1 in Appendix A. Thus, a possible deviation from isotropy could be quantified by plotting the ratio between $\overline{P}$ and the corresponding value of a test in, for instance, the L-direction (here denoted $\overline{P}_{L1}$) evaluated along the offset lines. Such ratios are plotted in Fig. 1 versus the offset line at which the specific ratio has been determined. Note that the case $i = L1$ is represented by a ratio equal to unity and is included for reference purposes. By comparing the normalized load ratios taken from tests in the same direction, a variation of about 0.005–0.01 can be observed. Hence, a deviation from unity must be larger than this in order to be significant. It can

Table 1
Material parameters for the mechanical properties of Weldox 420 and 960.

Material	σ_0 (MPa)	$R_{p0.2}$	R_m	$\bar{\varepsilon}_f^p$	N	ε_0	ε_s	ε_N
Weldox 420	418	415	525	1.44	0.180	0.0020	0.0084	0.0162
Weldox 960	956	996	1051	1.26	0.059	0.0046	0	0.0046

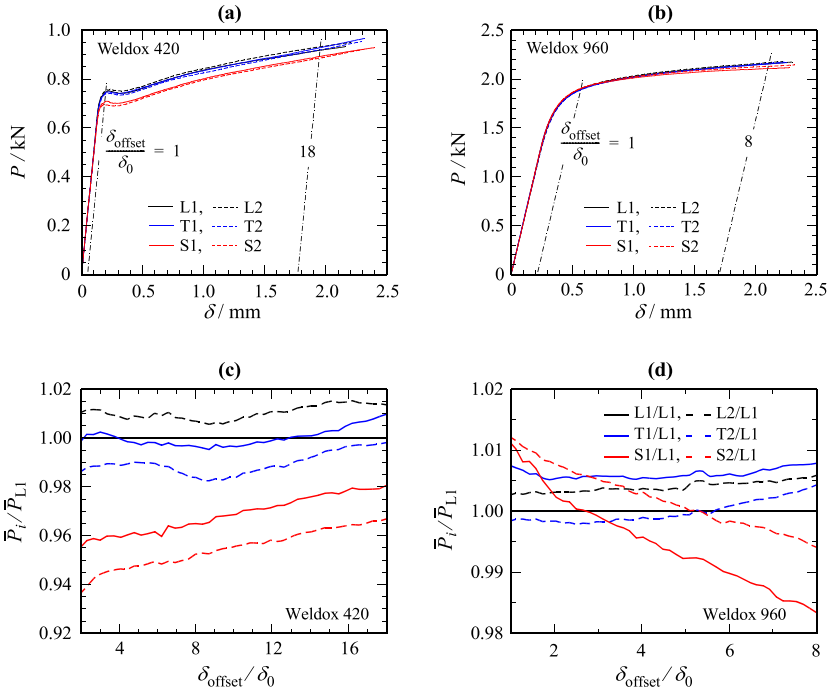

Fig. 1. Load–deflection curves from the bend tests executed in three perpendicular directions (L, T and S) for the materials Weldox 420 (a) and 960 (b), respectively. Normalized load ratios evaluated along a range in deflection offsets are shown for Weldox 420 (c) and 960 (d), respectively.

be seen that the assumption of isotropy is unambiguous for Weldox 960, as the deviation from unity of the normalized load ratios in Fig. 1(d) are insignificant. For Weldox 420 a minor deviation from unity may be judged to be significant in the S-direction. However, at the highest level of deformation ($\delta_{\text{offset}}/\delta_0 \geqslant 18$) the normalized load ratio for tests in the S-direction are in the range 0.97–0.98. Thus, the assumption of isotropy may be regarded as justified also for Weldox 420.

Further details regarding the materials such as microstructural properties and chemical composition are provided in Barsoum and Faleskog (2007a).

2.2. Test geometries and test procedures

Experimental results from tests on two different specimen geometries will be presented and summarized in the present paper. These are the double notched tube (DNT) specimen shown in Fig. 2(a–c) and the round notched bar specimen (RNB) shown in Fig. 2(e and f). The DNT specimens were subjected to a proportional combination of tension–torsion loading, and the RNB specimens to pure tensile loading.

The DNT specimen was grooved with two circumferential matching notches on the inner and outer surface as depicted in the close-up in Fig. 2(c), where the notch height $h = 1$ mm, the notch ligament thickness $t_n = 1.2$ mm, the thickness of the tube at the notch region $t = 3.2$ mm and the radius from the center of the tube to the center of the notch $R_m = 12$ mm. Other dimensions of interest are provided in Fig. B1 in Appendix B.

There are several reasons for introducing the notches into the DNT specimen: (i) the feasible range in triaxiality is expanded (for the present materials, the range in triaxiality is more than doubled if compared to a tube specimen with a smooth test section); (ii) problems such as buckling of a thin walled cylinder under shear is avoided, and hence, the extreme load cases of pure shear and pure tension can unambiguously be applied on the DNT specimen; (iii) plastic deformation as well as the onset of fracture processes will be confined to the notch region, which in some aspects simplify the evaluation of the tests as utilized here; (iv) finally, there is no need to introduce an imperfection in a numerical model to trigger the onset of localized deformation, as otherwise typically would be needed. The obvious drawback is that stress and strain fields are not homogeneous in the test section, and only quantities in an average sense may directly be evaluated from the present test geometry.

The DNT specimen was subjected to quasi-static loading by an axial force F and a torque M applied in proportion such that the ratio $\kappa = FR_m/M$ was kept constant during a test, with R_m being the radius to the middle of the notch of the undeformed specimen, see Fig. 2(c). The fixed load ratio κ is also equivalent to the ratio between the true normal stress and the true shear stress averaged over the net section plane between the notches, i.e., $\kappa = \bar{\sigma}_{\text{axial}}/\bar{\tau}_{\text{shear}}$, provided that R_m does not change much and that the notch ligament thickness remains small compared to R_m during loading, which was observed to be the case. Below, data will be presented in terms of

$$k_T = \frac{\kappa}{1+\kappa} = \frac{\bar{\sigma}_{axial}}{\bar{\sigma}_{axial} + \bar{\tau}_{shear}}, \tag{4}$$

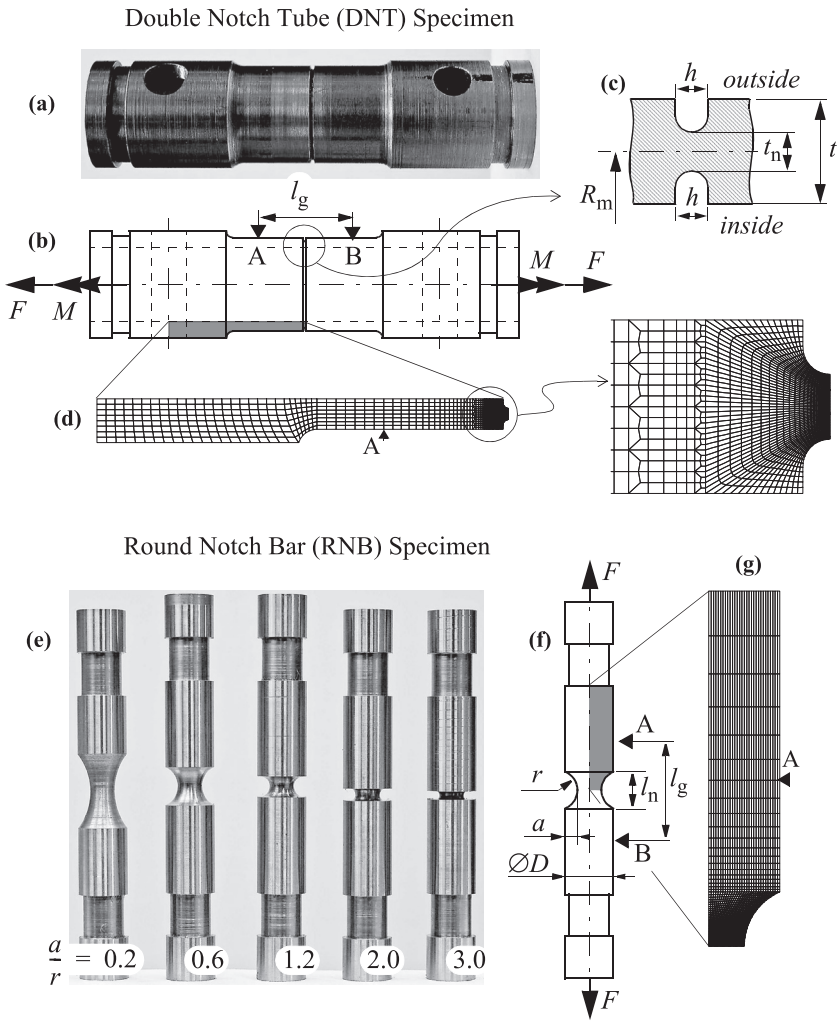

Fig. 2. Specimen geometries illustrated by photos, sketches indicating the applied loading and FEM meshes used in the analysis: DNT (a)–(d) and RNB (e)–(g), where the photo show specimen geometries for material Weldox 960.

and this is equal to zero in pure torsion and unity in pure tension. The stress triaxiality in the central part of symmetry plane between the notches will increase monotonically with k_T. However, as will be further discussed below, the deviatoric stress state parameter L will not undergo a monotonic change with k_T. As k_T increases from 0 to 1, L will change from 0 to -1 and back to 0 again, i.e., changing from a *shearing stress state* to an *axisymmetric state* and back to a *shearing stress state*. In Barsoum and Faleskog (2007a), 16 DNT specimens were tested in the range $0.38 \leqslant k_T \leqslant 1$ for Weldox 420 and 21 DNT specimens in the range $0.33 \leqslant k_T \leqslant 1$ for Weldox 960. In the present study, additionally 11 specimens of Weldox 420 and additionally 12 specimens of Weldox 960 were tested to cover the whole range down to $k_T = 0$, as seen by the summary of tests listed in Table B1 in Appendix B.

The DNT specimens were tested in a MTS servo-hydraulic tension–torsion two axis testing machine. The axial force was transmitted to the specimen through a loading device attached to the circumferential slots at the ends of the specimen, and torque was applied by pins attached to the specimen through the holes at the end of the specimen, see Fig. 2(a and b). Further details of the fixture used to mount the specimen into the MTS machine and the procedure to align a specimen are given in Appendix B. Testing was executed in deformation control by prescribing either the axial displacement or the twist angle (depending on the κ-value), and continuously adjusting the one not being prescribed such that proportional loading with a constant κ-value was maintained. This was done by an in-house written program connected to an Instron 8580 digital device controlling the MTS machine. During a test, the axial force, the torque, the axial displacement and the twist angle were continuously measured and stored digitally. The axial force and torque were measured by two independent load cells, where the relative errors in output from both load cells were less than 0.005. The axial displacement was measured over the gauge length $l_g = 26$ mm (the initial distance between points A and B in Fig. 2(b)) and taken as the average value from two Instron extensometers placed on each side of a specimen. The accuracy of the displacement measurement was about ±0.002 mm. The twist angle was measured over the same gauge length and evaluated from a clip-gauge, with a relative error in angle estimates less than 0.002 radians. Details of the experimental set-up can be seen in Fig. B2 in Appendix B. The measured axial displacement and twist angle will henceforth be referred to as δ_{ext} and θ_{ext}, respectively.

The RNB specimens were provided with a symmetrically placed circumferential notch of radius r. Five different a/r ratios were tested for each material. The tests and a/r ratios employed are summarized in Table B1 in Appendix B, where also tests from smooth round bars are included. The RNB specimens were mounted to a loading device by use of the circumferential slots at the ends of each specimen and tested in a servo-hydraulic testing machine. The axial load and the axial displacement between

points A and B in Fig. 2(f) were continuously measured during a test. The displacement was taken as the average measurement from two clip-gauges placed on each side of a specimen over the gauge length $l_g = 25$ mm (initial axial distance between points A and B). The dimensions of all specimens tested are given in Fig. B1 in Appendix B. Final failure by ductile fracture was in all tests preceded by the development of a neck, at which fracture commenced. After termination of each test, the average diameter of the neck was measured.

3. Evaluation procedures of experiments

The main purpose of the test program was to design a set of experiments that as clearly as possible brings out the effects of stress triaxiality and the deviatoric stress state on ductile failure. The DNT specimens tested in the whole range of combined tension–torsion available provides a set of highly discriminating tests. The RNB tests will then serve as a reference that probes the effect of stress triaxiality. Ductile failure is here quantified as the equivalent plastic strain to failure. It is possible to directly evaluate an average value of plastic strain from the experiments. However, certain steps must be taken to quantify the stress state. Here, the experiments were simulated by finite element calculations, where an isotropic material and standard finite strain J_2-plasticity theory was employed.

3.1. Evaluation of the overall equivalent plastic strain in the DNT-tests

To evaluate the overall equivalent plastic strain directly from the measurements of each DNT test, it was assumed that all plastic deformation is confined to the notch region. Thus, the plastic parts of the axial displacement and the twist angle over the notch, respectively, can be evaluated as

$$\delta_n^p = \delta_{\text{ext}} - C_\delta F, \quad \theta_n^p = \theta_{\text{ext}} - C_\theta M. \tag{5}$$

Here, C_δ and C_θ are elastic compliances over the gauge length between points A and B in Fig. 2(b). The elastic compliances were evaluated directly from the experimental data by use of the initial linear parts of the $F - \delta_{\text{ext}}$ and $M - \theta_{\text{ext}}$ records, respectively. As will be seen in Section 4, the measured values compared well with the theoretical compliances: $C_\delta = 1.112 \cdot l_g/(2\pi R_{\text{m}} tE)$ and $C_\theta = 1.070 \cdot l_g(1+\nu)/(\pi R_{\text{m}}^3 tE)$, which were calculated by the FEM analysis described below.

Accounting for finite strain effects, the overall axial and shear plastic strain rates over the notch can then be evaluated as

$$\dot{\varepsilon}_n^p = \frac{\dot{\delta}_n^p}{h+\delta_n}, \quad \dot{\gamma}_n^p = \frac{R_{\text{m}}\dot{\theta}_n^p}{h+\delta_n}, \tag{6}$$

where h is the initial notch (axial) height shown in Fig. 2(c) and δ_n is the current displacement over the notch estimated from the experimental measurements as

$$\delta_n = \delta_{\text{ext}} - C_{\delta l}F = \delta_{\text{ext}} - \frac{C_\delta}{1 + C_{\delta n}/C_{\delta l}}F. \tag{7}$$

The ratio between the axial displacement compliances $C_{\delta n}$ (over the notch height h) and $C_{\delta l}$ (over the gauge length excluding the notch h) were, contrary to C_δ , estimated from a linear elastic FEM calculation as $C_{\delta n}/C_{\delta l} = 0.06144$. By the assumption of plane strain conditions in the circumferential direction in the notch region and ignoring elastic strains (negligible compared to the plastic strains in all tests), the overall equivalent plastic strain over the notch can readily be written as

$$\bar{\varepsilon}_n^p = \int \dot{\bar{\varepsilon}}_n^p \mathrm{d}t \quad \text{with } \dot{\bar{\varepsilon}}_n^p = \frac{2}{\sqrt{3}}\sqrt{(\dot{\varepsilon}_n^p)^2 + (\dot{\gamma}_n^p/2)^2} \tag{8}$$

However, expression (8) is not optimal for integration of the two independent and indirect measured strain rate quantities in (6), due to small variations in signals or simply noise that inevitable will be present in experimental measurements. This was to some degree related to the control program and procedure used to apply proportional loading on a specimen as discussed above. Therefore, a slightly different and much more robust method for the integration of (8) was developed, where an effective displacement defined as $\delta_{\text{eff}} = \sqrt{\delta_{\text{ext}}^2 + (R_{\text{m}}\theta_{\text{ext}})^2}$ was introduced as a time like measure. The measurements of δ_n^p and θ_n^p in each test, respectively, were then fitted to N piecewise linear functions of δ_{eff}, where the extent of the linear functions were equidistant in δ_{eff}. The N point wise values of δ_n^p andθ_n^p (not counting the first being zero) used to establish the piecewise functions were estimated by taking the average of 6–8 data points below and above each of the N points (zero excluded). This turned out to be more reliable than using a least square fit to determine the N piecewise functions. Hence, the increments $\Delta\varepsilon_n^p$ and $\Delta\gamma_n^p$ could readily be evaluated over the N intervals, and integration of (8) for the estimation of the overall equivalent plastic strain over the notch was done as

$$\bar{\varepsilon}_n^p = \frac{2}{\sqrt{3}}\sum_{k=1}^{N}\sqrt{(\Delta\varepsilon_n^p)_k^2 + (\Delta\gamma_n^p/2)_k^2}. \tag{9}$$

Here, k refers to the interval number. With few exceptions, more than 2000 data points were recorded for each test, and N was chosen between 40 and 50, which was judged sufficient to obtain a sufficiently accurate result.

3.2. Evaluation of equivalent plastic strain for proportional deformation paths in combined stretching and shearing

As will be evident in Section 4, the development of the overall axial and shear plastic strain over the notch during a DNT test was fairly proportional. Based on this observation, a simple relation can be developed for the overall equivalent plastic strain over the notch. A cross-section of the notch region of the DNT specimen is sketched in Fig. 3(a), where a local Cartesian coordinate system is introduced. A planar surface initially parallel with the $\mathbf{e}_1$–$\mathbf{e}_3$ plane will deform as indicated by the thick line in Fig. 3(b), where the lower edge of the notch is used as the reference point of departure. Connecting the experimental quantities with the displacements introduced in Fig. 3(b), δ_1 corresponds to δ_n and δ_2 to $R_{\text{m}}\theta_n$, respectively. Locally, the deformation field in the notch can then be characterized as illustrated in Fig. 3(c). And hence, across the notch, the average stretch and the average shearing are given by

$$\lambda = \frac{h+\delta_1}{h}, \quad k = \lambda\tan\varphi_n = \frac{\delta_2}{h}, \tag{10}$$

where φ_n represents the average shear angle over the notch, as sketched in Fig. 3(b). By neglecting elastic compressibility and assuming plane strain conditions in the direction of $\mathbf{e}_2$ (elastic deformation prevails outside the notch and the circumference $2\pi R_{\text{m}}$ can for this reason be assumed to be inextensible and as a result the stretch in the circumferential direction is set to unity), the resulting average deformation gradient over the notch can be expressed as $\mathbf{F} = \lambda\mathbf{e}_1\otimes\mathbf{e}_1 + \mathbf{e}_2\otimes(k\mathbf{e}_1 + \mathbf{e}_2) + \lambda^{-1}\mathbf{e}_3\otimes\mathbf{e}_3$, with $\mathbf{e}_i$ being the Cartesian basis vectors introduced in Fig. 3. The rate of deformation and its additive decomposition into an elastic and plastic part then becomes

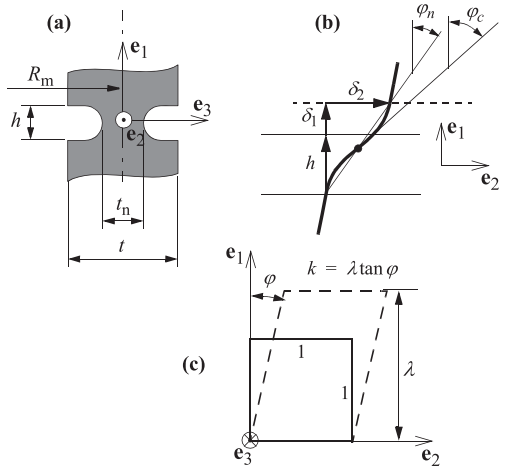

Fig. 3. (a) A section of the notch region of a DNT specimen (neglecting the curvature) subjected to a combined tensile and shear load, giving rise to a normal displacement δ_1 and a shear displacement δ_2 depicted in (b), which is simplified to combined stretching and shearing of a material unit as depicted in (c).

$$\mathbf{d} = \frac{1}{\lambda}\begin{bmatrix} \dot\lambda & \dot k/2 & 0 \\ \dot k/2 & 0 & 0 \\ 0 & 0 & -\dot\lambda \end{bmatrix} = \frac{1}{\lambda}\begin{bmatrix} \dot\lambda_e & \dot k_e/2 & 0 \\ \dot k_e/2 & 0 & 0 \\ 0 & 0 & -\dot\lambda_e \end{bmatrix} + \frac{1}{\lambda}\begin{bmatrix} \dot\lambda_p & \dot k_p/2 & 0 \\ \dot k_p/2 & 0 & 0 \\ 0 & 0 & -\dot\lambda_p \end{bmatrix} = \mathbf{d}_e + \mathbf{d}_p. \tag{11}$$

Based on the plastic part of (11), the equivalent plastic strain rate can be expressed as

$$\dot{\bar\varepsilon}^p = \frac{2}{\sqrt{3}}\sqrt{\left(\frac{\dot\lambda_p}{\lambda}\right)^2 + \left(\frac{\dot k_p}{2\lambda}\right)^2}. \tag{12}$$

To proceed, we neglect the elastic contribution to the stretch ($\lambda \approx \lambda_p$) and consider a proportional path of deformation such that $\dot\lambda_p/(\dot k_p/2) = (\lambda_p - 1)/(k_p/2) =$ constant. Integration of the rate Eq. (12) then gives a relation for the equivalent plastic strain for a proportional path as

$$\begin{aligned}\bar\varepsilon^p_{\text{prop}} &= \frac{2}{\sqrt{3}}\sqrt{(\lambda_p - 1)^2 + \left(\frac{k_p}{2}\right)^2}\,\frac{\ln\lambda_p}{\lambda_p - 1} \\ &= \frac{2}{\sqrt{3}}\sqrt{(\lambda_p - 1)^2 + \left(\frac{k_p}{2}\right)^2}\left[1 + \sum_{n=1}^{\infty}\frac{(-1)^n}{1+n}(\lambda_p - 1)^n\right].\end{aligned} \tag{13}$$

The extreme cases are obtained as $\bar\varepsilon^p_{\text{prop}} = k_p/\sqrt{3}$ in pure torsion ($\lambda_p = 1,\ k_T = 0$) and $\bar\varepsilon^p_{\text{prop}} = (2/\sqrt{3})\ln\lambda_p$ in pure tension ($k_p = 0,\ k_T = 1$). From (10), the plastic stretch and plastic shearing in (13) are seen to be related to the experimental measurements as

$$\lambda_p = 1 + \frac{\delta^p_n}{h} \quad \text{and} \quad k_p = \frac{R_m\theta^p_n}{h}, \tag{14}$$

where δ^p_n and θ^p_n are defined in (5). In addition to expression (9), relation (13) will also be used to evaluate the overall equivalent plastic strain over the notch in the DNT tests. The deformation gradient description used here bear a close resemblance with the kinematic description introduced by the authors in Barsoum and Faleskog (2007b) and more recently a similar representation is used in Haltom et al. (2013).

In view of the experimental results to be presented below, it is of interest to check the accuracy of (13) in the presence of a nonlinear deformation history. For this purpose, stretch and shearing are parameterized by a non-dimensional loading parameter $\xi(\dot\xi > 0)$ in the range zero to unity as follows

$$\begin{cases} \lambda - 1 = \xi(\lambda_C - 1) - \xi(1-\xi)4\Delta\sin\beta \\ \frac{k}{2} = \xi\frac{k_C}{2} + \xi(1-\xi)4\Delta\cos\beta \end{cases} \text{with} \begin{cases} \Delta = \eta\sqrt{(\lambda_C - 1)^2 + (k_C/2)^2} \\ \beta = \arctan\left(\frac{k_C}{2(\lambda_C - 1)}\right) \end{cases} \tag{15}$$

In (15), λ_C and k_C represents the end values of the deformation path and parameter η quantifies the degree of nonlinearity of the deformation history, as depicted in Fig. 4(a). Again neglecting the elastic deformation and inserting (15) into (12), numerical integration of (12) then gives an equivalent plastic strain that accounts for the nonlinearity in the deformation path, henceforth denoted $\bar\varepsilon^p_\eta$. Hence, the accuracy of (13) in the presence of a nonlinear deformation history can be assessed in terms of η as shown in Fig. 4(b–d). Here, the relative error, defined as $\bar\varepsilon^p_{\text{prop}}/\bar\varepsilon^p_\eta - 1$, is plotted versus $\bar\varepsilon^p_\eta$ for the range $-0.08 \leqslant \eta \leqslant 0.08$ and for the three cases: $\beta = 0^\circ$ ($k_C = 0$), $\beta = 90^\circ$ ($\lambda_C = 1$) and $\beta = 30^\circ$. It can be observed that relation (13) is very accurate and essentially independent of the amount of plastic deformation ($\bar\varepsilon^p_\eta$) for the stretch dominated case ($\beta = 0^\circ$) shown in Fig. 4(b) even for η values as high as ± 0.08, for which the relative error is less than 2%. As β increases from zero and shearing comes into play, the relative error starts to display a significant influence of $\bar\varepsilon^p_\eta$ (since Δ starts to affect λ), which is most clearly seen for the case dominated by shearing ($\beta = 90^\circ$) presented in Fig. 4(d). But, also in this case the relative error stays within a few percent for the range considered in $\bar\varepsilon^p_\eta$, provided that $|\eta| \leqslant 0.04$. This is as well valid for the high value of nonlinearity $|\eta| = 0.08$, if $\bar\varepsilon^p_\eta$ is less than about 0.4, as observed in Fig. 4(d). But, as $\bar\varepsilon^p_\eta$ increase for this high value of nonlinearity, the relative error also increases and becomes similar to $|\eta|$ in value at $\bar\varepsilon^p_\eta \approx 1.5$.

For cases of combined stretching and shearing in between the extreme cases, the relative error changes in a rather monotonic manner from what can be observed for the stretching case in Fig. 4(b) to reach a maximum for the shearing case in Fig. 4(d). This is illustrated for the intermediate case displayed in Fig. 4(c), where $\beta = 30^\circ$. In this context, note that the relative error is independent of β in the limit $\bar\varepsilon^p_\eta \to 0$. Furthermore, relation (13) may overestimate the equivalent plastic strain for deformation paths with negative η values, if $\bar\varepsilon^p_\eta$ is sufficiently large. This is because the stretch in the incremental form (12) used to calculate $\bar\varepsilon^p_\eta$, attains a larger value over a relatively larger portion of the deformation path as compared to the proportional deformation path assumed for relation (13). In conclusion, relation (13) is anticipated to give fairly accurate estimations for the equivalent plastic strain at failure in the presence of moderate nonlinearities in the deformation history as will be evident below.

3.3. Strain and stress state: plane strain tension combined with simple shear

The average stress state over the net section between the notches in a DNT specimen will now be assessed in an approximate way. As a starting point, consider once again the notch section displayed in Fig. 3(a), where plane strain conditions are assumed in the $\mathbf{e}_2$-direction. As in the previous Section, elastic strains are neglected and it is assumed that the material follow a standard J_2 flow theory of plasticity. Then, the stresses averaged over the net section plane between the notches may be approximated by

$$\sigma_{11} = \sigma, \quad \sigma_{22} = (1+\mu)\sigma/2, \quad \sigma_{33} = \mu\sigma, \quad \sigma_{12} = \tau. \tag{16}$$

A remark is here in place: the presence of the notches will on the average generate a normal stress in the $\mathbf{e}_3$-direction that is proportional to σ and depends on κ, and this is accounted for by the dimensionless parameter μ introduced in (16). Recall that the load ratio $\sigma/\tau = \kappa$ is prescribed and kept constant in the DNT tests. From (16), the principal stresses can be evaluated as

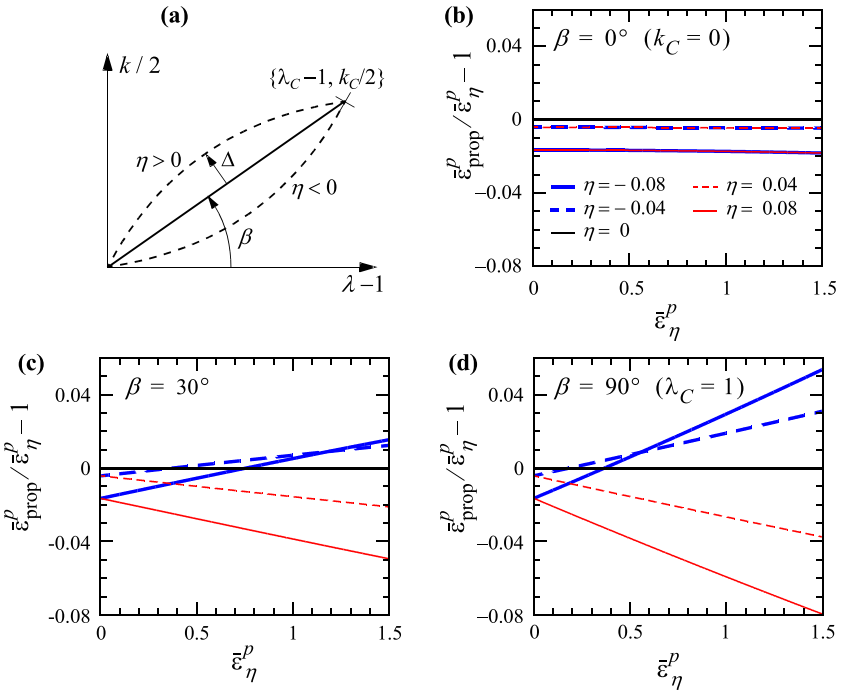

Fig. 4. (a) Definition of a non-linear deformation path in the stretch and shearing space parameterized by η. Relative error in equivalent plastic strain due a non-linear deformation path for (b) $\beta = 0^\circ$, (c) $\beta = 30^\circ$, and (d) $\beta = 90^\circ$.

$$\sigma_I = \tfrac{3+\mu}{4}\sigma + \sqrt{\left(\tfrac{1-\mu}{4}\right)^2\sigma^2 + \tau^2}$$

$$\sigma_{II} = \mu\sigma, \quad \sigma_{III} = \tfrac{3+\mu}{4}\sigma - \sqrt{\left(\tfrac{1-\mu}{4}\right)^2\sigma^2 + \tau^2} \quad \text{for } \sigma < \tau\sqrt{2}/(1-\mu)$$

$$\sigma_{II} = \tfrac{3+\mu}{4}\sigma - \sqrt{\left(\tfrac{1-\mu}{4}\right)^2\sigma^2 + \tau^2}, \quad \sigma_{III} = \mu\sigma \quad \text{for } \sigma > \tau\sqrt{2}/(1-\mu) \tag{17}$$

Note that, both in pure torsion ($\sigma = 0 \Rightarrow \sigma_I = -\sigma_{III} = \tau,\ \sigma_{II} = 0$) and in pure tension ($\tau = 0 \Rightarrow \sigma_I = \sigma,\ \sigma_{II} = (1+\mu)\sigma/2,\ \sigma_{III} = \mu\sigma$), a shearing stress state prevails, i.e., $L = 0$ and $\omega = 1$. In between the extreme load cases, the stress state will at a certain stage become axisymmetric ($L = -1$ or $\omega = 0$), which occurs when $\sigma_{II} = \sigma_{III}$. It follows from (17) that this will take place when the inverse load ratio $1/\kappa = \tau/\sigma = (1-\mu)/\sqrt{2}$. Moreover, when the stress state is axisymmetric, the deviatoric stress components $s_{11} = (1-\mu)\sigma/2$ and $s_{12} = \tau$, and hence the ratio s_{11}/s_{12} becomes equal to $1/\sqrt{2}$. By recourse to the assumption of an associated flow rule, an axisymmetric state of loading is expected to prevail when the ratio between plastic normal strain and shear strain over the notch takes on the value

$$\frac{\dot{\varepsilon}_n^p}{\dot{\gamma}_n^p/2} = \frac{\dot{\lambda}_p}{\dot{k}_p/2} = \frac{1}{\sqrt{2}}. \tag{18}$$

3.4. FEM analysis for evaluation of stress state parameters

Accurate full scale elastic–plastic three-dimensional finite element calculations based on the Gurson constitutive model modified for shear failure (Nahshon and Hutchinson, 2008) will be presented in Part II for both the DNT tests and the RNB tests. Here, a FEM analysis limited to an axisymmetric combination of axial extension and torsion and based on a standard finite strain J_2 flow theory of plasticity were carried out to estimate the stress triaxiality, T, and the deviatoric stress state parameters L and ω in the two types of tests. The FEM calculations were done by use of the program ABAQUS (2010) adopting quadratic elements with reduced integration. Typical meshes used in the calculations of the DNT and RNB specimens are shown in Fig. 2(d and g). In the DNT mesh, 60 equally sized elements were used across the notch ligament t_n. Thus, elements of size 20×20 μm were employed in the notch region in the plane shown in the close-up of Fig. 2(d). Similar sized element was also used in the notch region of a typical RNB mesh. Proportional loading in the DNT geometries were accomplished by employing a technique based on master/slave nodes combined with a suitable coordinate transformation similar to the method described in Gao et al. (1998). This was accomplished by a user subroutine implemented into ABAQUS (2010).

4. Experimental results and discussion

4.1. General results from the DNT tests

Experimental load–displacement records for a representative set of DNT tests are shown in Fig. 5(a and b) for steel Weldox 420 and in Fig. 6(a and b) for steel Weldox 960. In sub-figures (a) the axial force, F, is plotted versus the axial displacement,δ_{ext}, and in sub-figures (b) the torque, M, versus twist angle, θ_{ext}, are plotted for the corresponding tests. The initial compliances, used to evaluate the plastic part of deformation in Eq. (5), agreed quit well with the theoretical value presented in Section 3.1. Here, the deviation from the theoretical compliance value in torsion was in the whole range of κ within ±6% except in a few cases, and the deviation from the theoretical compliance in tension was typically within ±10% load cases dominated by tension.

The interruption of each curve in Figs. 5 and 6 represents the point of complete specimen failure, and in all tests, without exception, failure occurred in the post peak load regime. In tests conducted at higher values of the load ratio, i.e., $k_T \approx 0.65$ or higher (spec. No. 119–127 and 220–233), failure occurred abruptly in the post peak load regime after a certain amount of a slow decay in load level. This decay in load level was primarily associated with

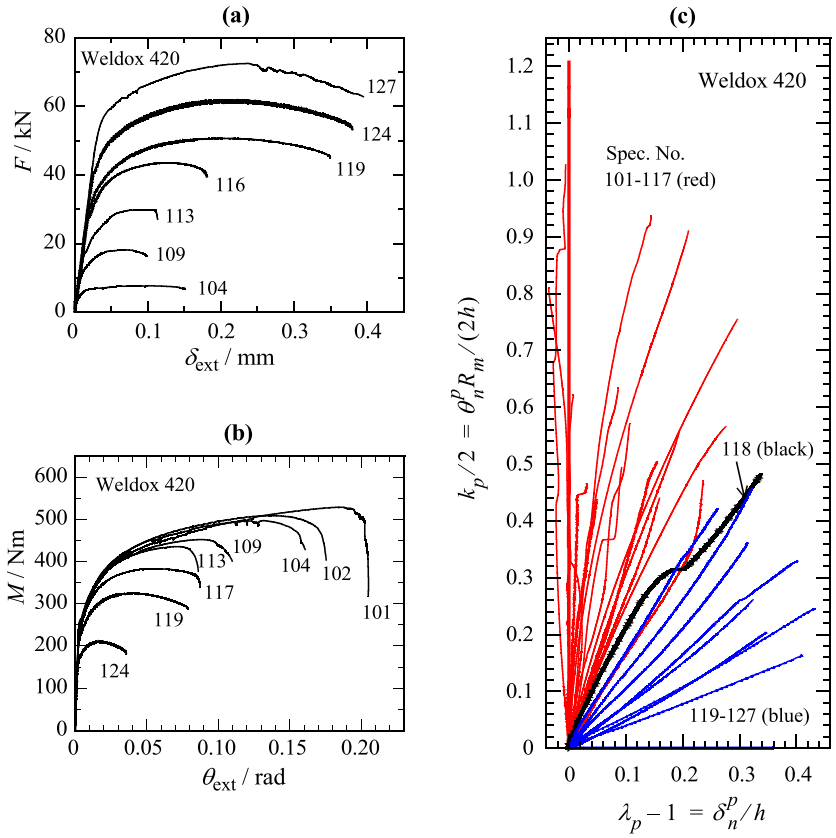

Fig. 5. Experimental results for Weldox 420 showing (a) tensile load F versus displacement δ_{ext}, (b) torque M versus twist angle θ_{ext}, and (c) plastic stretching and shearing paths over the notch region.

a diffuse decrease in the net section area between the notches characterized by a rather smooth geometrical change (diffuse necking) occurring at a scale set by the notch height. In these tests, failure then developed in an unstable manner due to a rapid progression of damage, characterized by nucleation, growth and coalescence of voids. The latter was concluded from a thorough SEM examination of the fracture surfaces, which is described in Barsoum and Faleskog (2007a); see Figs. 13(c) and 14(c) therein. The diffuse decrease in the net section area mentioned above was also observed in and captured by the FEM analysis of the DNT tests based on a finite strain J_2 plasticity theory. The load–deformation curves from the FEM analysis are shown in Fig. 7, and as can be observed for the higher values of k_T, the agreement with the corresponding experimental curves displayed in Figs. 5 and 6 is good both in qualitative and quantitative terms.

By contrast, Fig. 7 shows that the FEM analysis did not predict a load maximum prior to failure, in tests performed at the lower load ratios, say $k_T < 0.50$. However, such load maxima are observed in the corresponding experimental curves, cf. Figs. 5(a and b) and 6(a and b). Thus, the softening observed in these experiments was not due to a diffuse decrease in the net section area. Instead, it is anticipated that the primary cause of softening was due to the development of damage, which at least in the shearing limit ($k_T = 0$) leads to localization. This is supported by the careful SEM examinations of some of the tests in the low range of k_T, see Figs. 13(a) and 14(a) in Barsoum and Faleskog (2007a). There, it was clear that the progression of damage was associated with flattening of voids that rotate and start to interact in a manner that leads to coalescence and final failure. As will be discussed below, the orientation of the overall planes of fracture can be rationalized by the orientation of conceivable bands of plastic localization. It is plausible that the very sharp but stable decrease in load level seen in some experiments dominated by torsion is due plastic shear localization spreading across the notch. But, it should be noted that the additional increment in displacement associated with such a sharp and stable load drop is very limited compared to the total plastic deformation preceding failure, and this had minimal effect on the evaluation of the overall equivalent plastic strain over the notch at failure by Eq. (9). A fairly thorough discussion on the onset of localization and its relation to the macroscopic strain is given in Section 3.2 of Part II.

In Figs. 5(c) and 6(c), the plastic parts of the deformation measures over the notch evaluated as defined in (5) are plotted against each other. Both measures are normalized as suggested in (14) Such that the quantities plotted represent the plastic stretch and plastic shearing. Note that almost all curves are essentially linear, i.e., that the paths of deformation of the overall plastic normal strain and plastic shear strain over the notch are in essence also proportional like the stress paths. Color red corresponds to deformation histories with ratio $2(\lambda_p - 1)/k_p$ below $1/\sqrt{2}$ and color blue to deformation histories above $1/\sqrt{2}$. Recall from the discussion in Section 3.3 that for $2(\lambda_p - 1)/k_p \approx 1/\sqrt{2}$ the state of deformation can be expected to be axisymmetric under proportional loading conditions.

The quotient between the overall plastic normal strain rate and plastic shear strain rate averaged over the deformation paths shown in Figs. 5(c) and 6(c) are plotted versus the normalized load ratio, k_T , in Fig. 8. Included, is also the corresponding result from the finite element simulations. Apart from a noticeable scatter in the experimental data, the experimental data follow the trend of

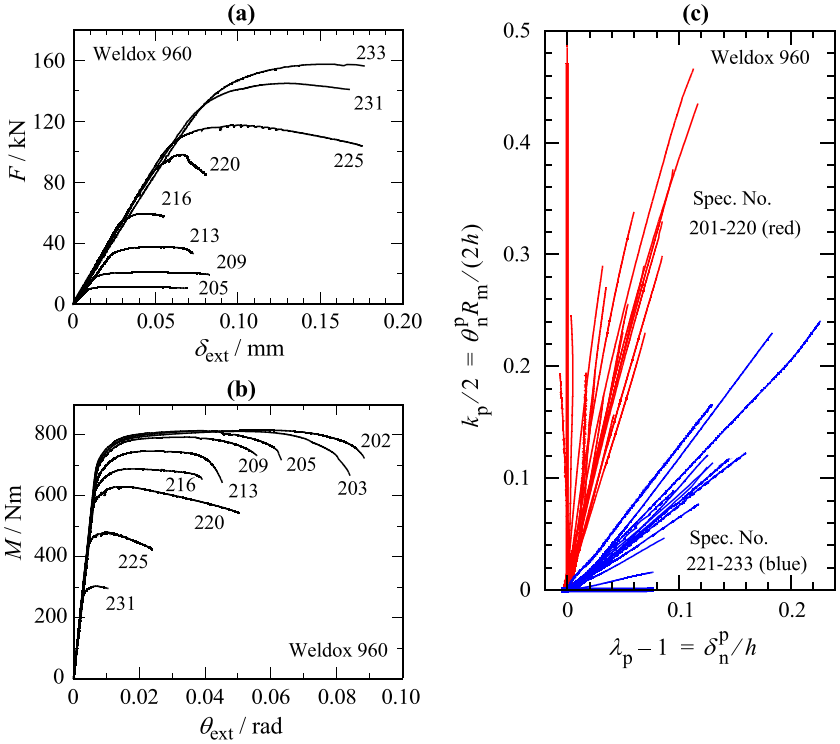

Fig. 6. Experimental results for Weldox 960 showing (a) tensile load F versus displacement δ_{ext}, (b) torque M versus twist angle θ_{ext}, and (c) plastic stretching and shearing paths over the notch region.

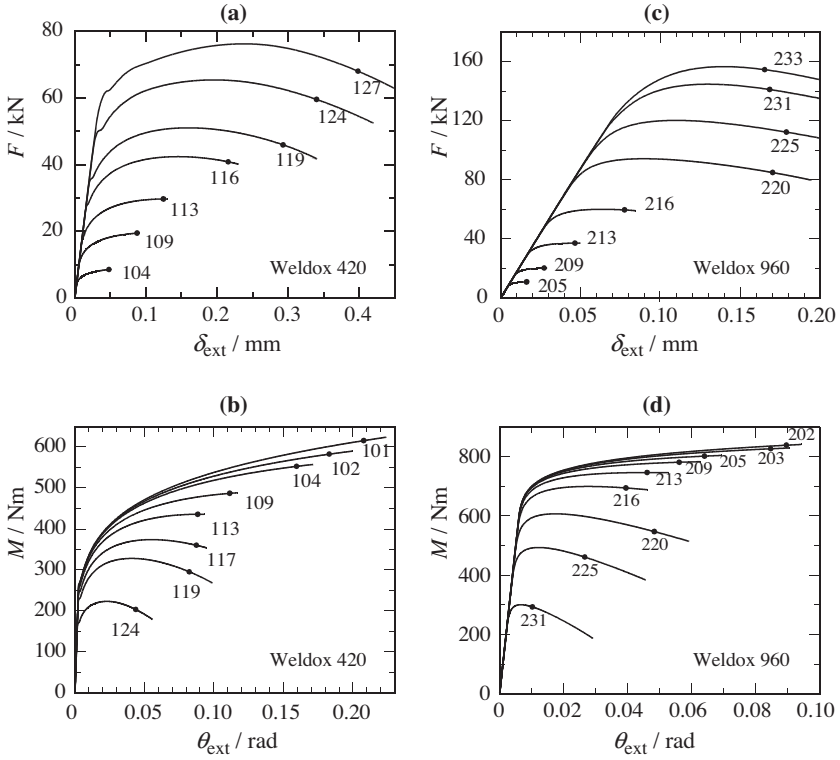

Fig. 7. Results from the axisymmetric FEM analysis are shown for Weldox 420 in (a) and (b) and for Weldox 960 in (c) and (d), where F versus δ_{ext} curves are plotted in (a) and (c), and M versus θ_{ext} curves are plotted in (b) and (d). The symbols indicate the point of failure in the tests, defined as the point where the overall plastic strain over the notch, evaluated from the results of the FEM analysis by use of Eq. (7), equaled the corresponding experimental value at failure.

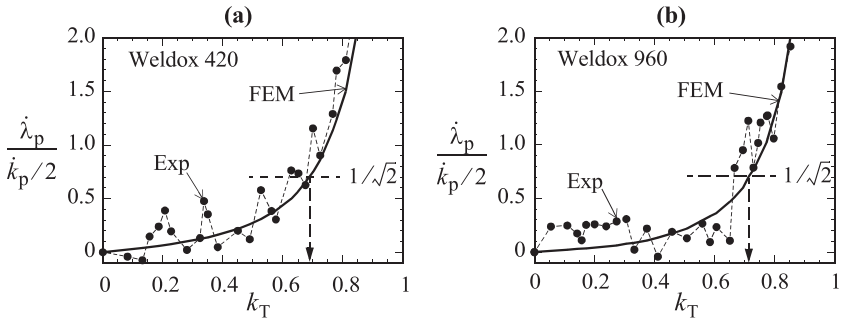

Fig. 8. Average plastic strain ratios over the notch in the DNT tests for steels Weldox 420 (a) and 960 (b), respectively.

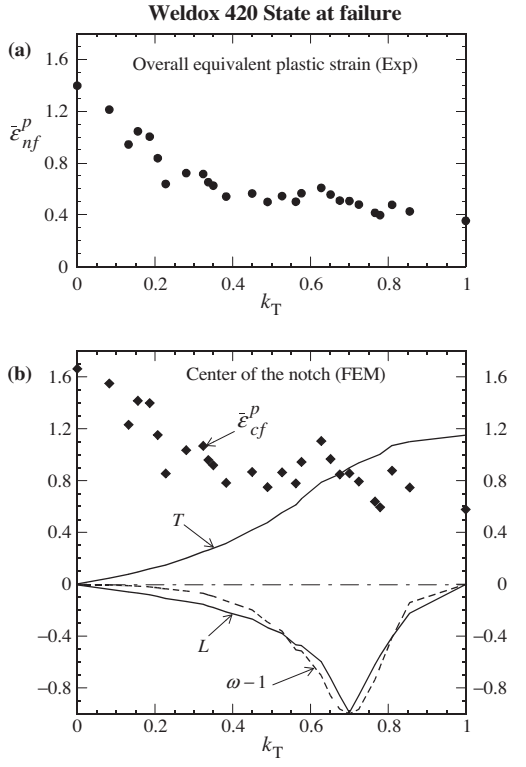

Fig. 9. (a) Overall equivalent plastic strain evaluated directly from experimental measurements versus normalized load ratio k_T, (b) FEM results extracted from the center of the notch region versus k_T. All results belong to material Weldox 420.

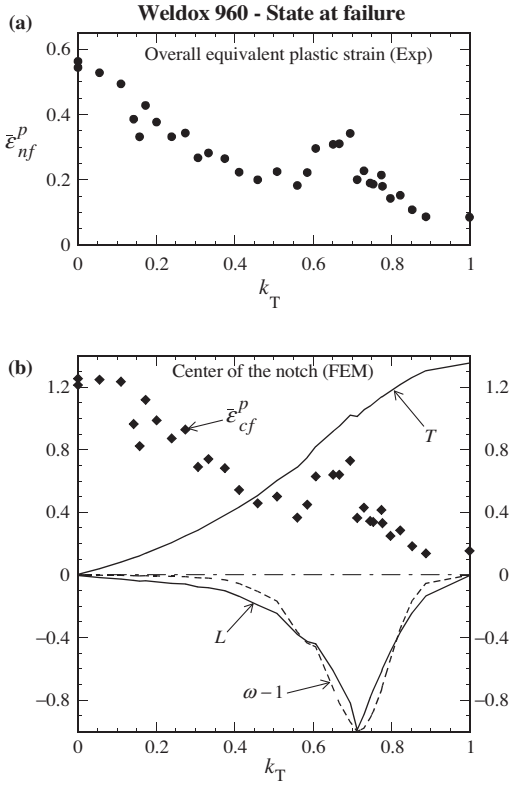

Fig. 10. (a) Overall equivalent plastic strain evaluated directly from experimental measurements versus normalized load ratio k_T, (b) FEM results extracted from the center of the notch region versus k_T. All results belong to material Weldox 960.

the FEM solutions fairly well, and this is valid for both materials. As discussed above, an axisymmetric stress state prevails when the strain rate ratio is equal to $1/\sqrt{2}$. From the data shown in Fig. 8, this occurs at $k_T \approx 0.7$ (slightly below for Weldox 420 and slightly above for Weldox 960). This observation will be pivotal for how to interpret the trends observed for the strain to failure to be discussed next.

4.2. Strain at failure in DNT tests

The key results from the tests, the equivalent plastic strain at failure versus the normalized loading ratio, k_T, is shown in Fig. 9 for Weldox 420 and in Fig. 10 for Weldox 960. Here, the symbols represent the DNT tests listed in Table B1 in Appendix B. The results shown in sub-figures (a) pertain to data directly extracted from the experiments. Thus, in Figs. 9(a) and 10(a) the overall equivalent plastic strain at failure $\bar{\varepsilon}^p_{nf}$ is shown, evaluated according to Eq. (9) and the procedure underpinning it. The results displayed in sub-figures (b) correspond to results from the finite element simulations evaluated at the instant of failure, taken as the point in loading where $\bar{\varepsilon}^p_n$, evaluated in the exact same way as in the experiments, matched the value at failure in the particular test that was simulated, i.e., $\bar{\varepsilon}^p_{nf}$. Here, the equivalent plastic strain, the stress triaxiality T, the Lode parameter L and the parameter $\omega - 1$, all evaluated at the center of the ligament between the notches, are plotted versus k_T. The equivalent plastic strain in the center at failure is here denoted $\bar{\varepsilon}^p_{cf}$. It is reasonable to use the center value, as the onset of failure in most cases initiated there.

Note that Figs. 9(b) and 10(b) clearly show that triaxiality increases in a monotonic manner as k_T increases from zero in pure torsion to unity in pure tension. To be specific, T increases from zero to 1.15 in the tests on Weldox 420, and from zero to 1.35 in the tests on Weldox 960, respectively. It can be observed that both materials expose a sensitivity to T, such that a general increase in equivalent plastic strain at failure is noted as T decreases from its maximum value down to zero as normally would be expected. But, most importantly, it is clear that the overall equivalent plastic

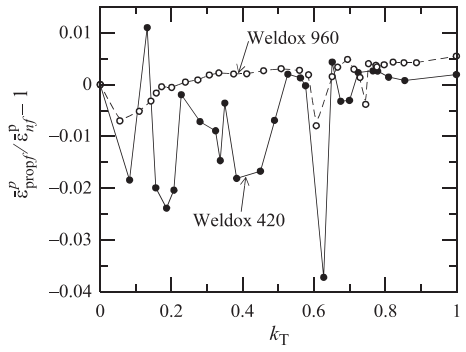

Fig. 11. Relative error in the overall equivalent plastic strain evaluated by Eq. (13), which is based on the assumption of a proportional plastic deformation path, versus load ratio k_T for the two steels Weldox 420 and 960.

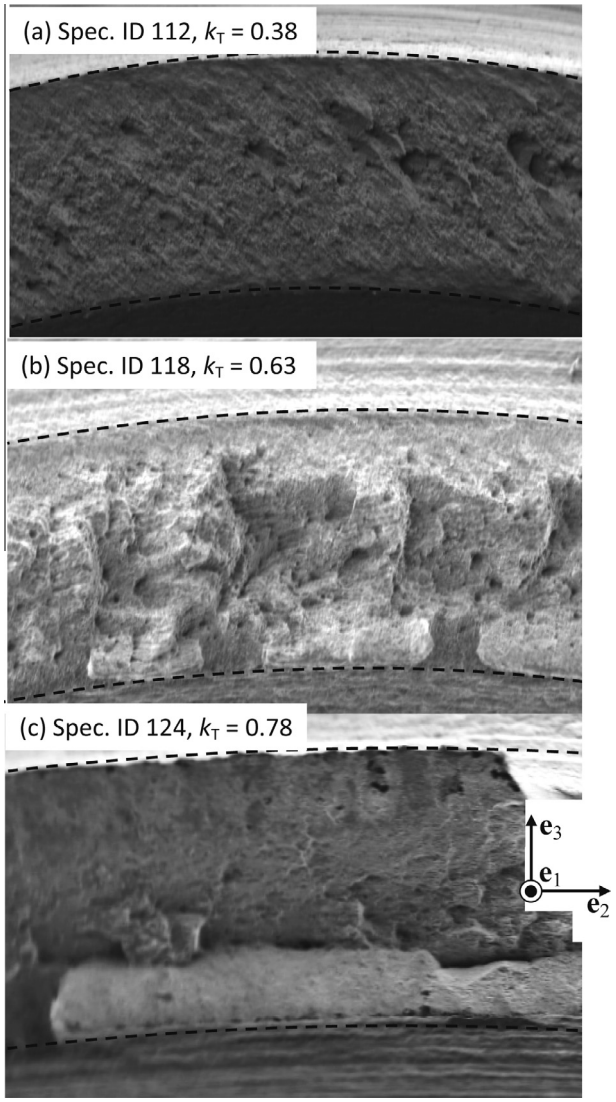

Fig. 12. SEM pictures of fracture surfaces taken from different DNT tests on material Weldox 420 subjected to loading ratios: (a) $k_T = 0.38$, (b) $k_T = 0.63$, (c) $k_T = 0.78$.

strain at failure $\bar{\varepsilon}^p_{nf}$ in sub-figures (a) is not a monotonic function of k_T, and thus not a monotonic function of T, and this is valid for both materials. This trend is even more pronounced for $\bar{\varepsilon}^p_{cf}$, as seen in sub-figures (b). A most interesting feature is that both $\bar{\varepsilon}^p_{nf}$ and $\bar{\varepsilon}^p_{cf}$ exhibits a cusp. For Weldox 960 the cusp is located at $k_T \approx 0.7$, where an axisymmetric stress state is expected to prevail, as confirmed by the L- and ω-curves shown in Fig. 10(b). As k_T decreases from 0.7, L rapidly approaches zero and thus the stress state approaches a shearing state, which is more severe from a ductility point of view. To conclude the behavior in the whole range of k_T: as the loading ratio decrease from unity to about 0.7, the decrease in T and L cooperates to enhance $\bar{\varepsilon}^p_{nf}$ (or $\bar{\varepsilon}^p_{cf}$); as k_T further decreases from 0.7 towards zero, the effect on $\bar{\varepsilon}^p_{nf}$ of a further decrease in T is initially defeated by a rapid increase in L that reduces $\bar{\varepsilon}^p_{nf}$. However, as the rate of change of L weakens, $\bar{\varepsilon}^p_{nf}$ starts to pick up again to reach its maximum value in pure shear for $k_T = 0$. A similar trend can be observed for Weldox 420, except that the cusp is shifted somewhat below the load ratio corresponding to the axisymmetric stress state. Finally, by comparing the failure strain curves in Figs. 9 and 10, it can be observed that the sensitivity for a change in the deviatoric stress state is much more pronounced for the high strength and low hardening steel Weldox 960 than it is for Weldox 420. For instance, the quotient between the cusp value and the minimum value in the valley in Fig. 10(a) is close to 1.8, whereas it is only about 1.2 in Fig. 9(a).

The validity of relation (13), based on the assumption of proportional straining, was checked for all the tests listed in Table B1 in the Appendix B. This was accomplished by first calculating the values of λ_p and k_p by use of Eq. (14) and the records of δ^p_n and θ^p_n at failure. The resulting value of the overall equivalent plastic strain at failure resulting from (13) is here denoted $\bar{\varepsilon}^p_{propf}$. A comparison of $\bar{\varepsilon}^p_{propf}$ with the more accurate valued based on Eq. (9), i.e., $\bar{\varepsilon}^p_{nf}$, is presented in Fig. 11, where the relative error, $\bar{\varepsilon}^p_{propf}/\bar{\varepsilon}^p_{nf} - 1$, is plotted versus the normalized loading ratio k_T. As can be observed in Fig. 11, the relative error is with a few exceptions less than ± 0.5% for Weldox 960, which is a consequence of the highly proportional deformation paths observed for this material, cf. Fig. 6(c). For Weldox 420, the relative error is in most cases between 0.5% and −2%. This would indicate that a slight deformation path nonlinearity, primary of the type $\eta > 0$ shown in Fig. 4(a), are present in some of the tests. The latter is to some extent qualitatively supported by the appearance of the deformation paths shown in Fig. 5(c).

At this junction a comment is in place. The method employed to evaluate the overall equivalent plastic strain presented for the limited range of DNT tests presented in Barsoum and Faleskog (2007a) was essentially based on direct integration of Eq. (8), which is a less robust method than the one presently used. Therefore, some of the $\bar{\varepsilon}^p_{nf}$ values given in Barsoum and Faleskog (2007a) were up to 10% higher than the corresponding, and more correct, values presented here.

4.3. Planes of failure and fracture surfaces in DNT tests

Scanning electron microscope pictures of fracture surfaces from three different test specimens of Weldox 420 are shown in Fig. 12. To interpret these pictures, it is enlightening to connect to Fig. 9, where the equivalent plastic strain at failure is plotted versus normalized loading ratio k_T. The pictures in Fig. 12 illustrate characteristic features of the surface morphology and planes of fracture for tests with (a) a k_T value below the cusp, (b) at the cusp and (c) above the cusp, respectively, seen in the $\bar{\varepsilon}^p_{nf}$ versus k_T curve shown in Fig. 9. The dashed lines in each picture delineates the contours of the notch ligament, which gives a sense of scale, since the distance between the dashed lines was 1.2 mm in the un-deformed state. As will be evident below, the orientation of the planes of rupture can be rationalized by how planes of localized plastic deformation would be presumed to be oriented. The normal to a plane of plastic localization is expected to be perpendicular to the direction of the

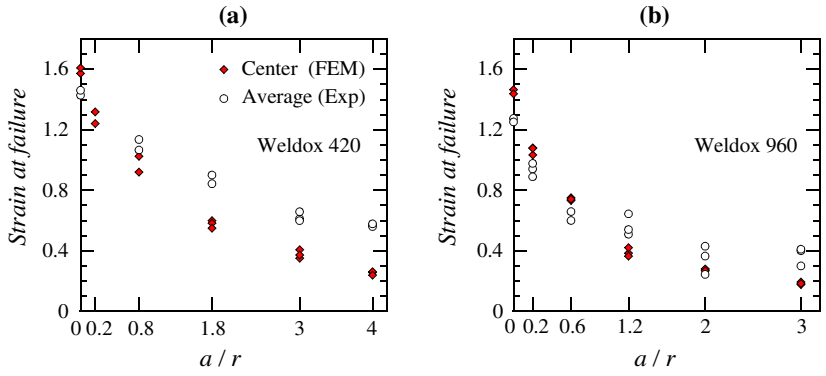

Fig. 13. Equivalent plastic strain at failure in tests on RSB ($a/r = 0$) and RNB specimens with different notch depth over notch radius ratios, a/r, evaluated from the reduction of cross sectional area measured on fractured specimens (open symbol) and from FEM results evaluated in the center of the neck region at the instant of failure (filled symbol) for materials: (a) Weldox 420 and (b) Weldox 960.

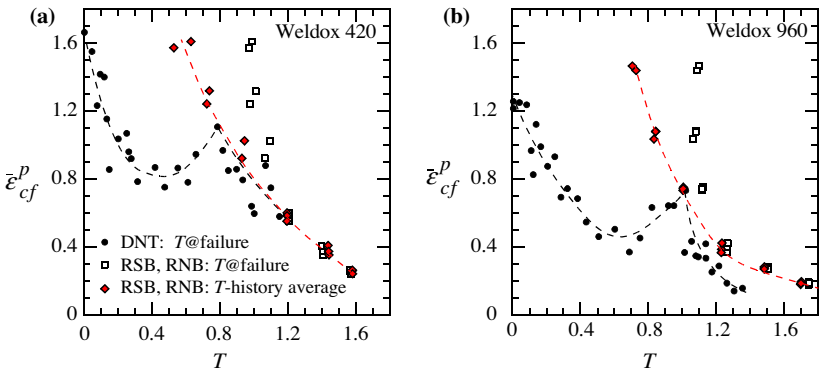

Fig. 14. Comparison between DNT, RSB and RNB specimens showing equivalent plastic strain at failure, $\bar{\varepsilon}^p_{cf}$, in the center of the grooved region versus stress triaxiality, T. The results are based on FEM analysis. The data in (a) belongs to tests on Weldox 420, and in (b) to Weldox 960. The dashed lines are included to aid the interpretation of the data.

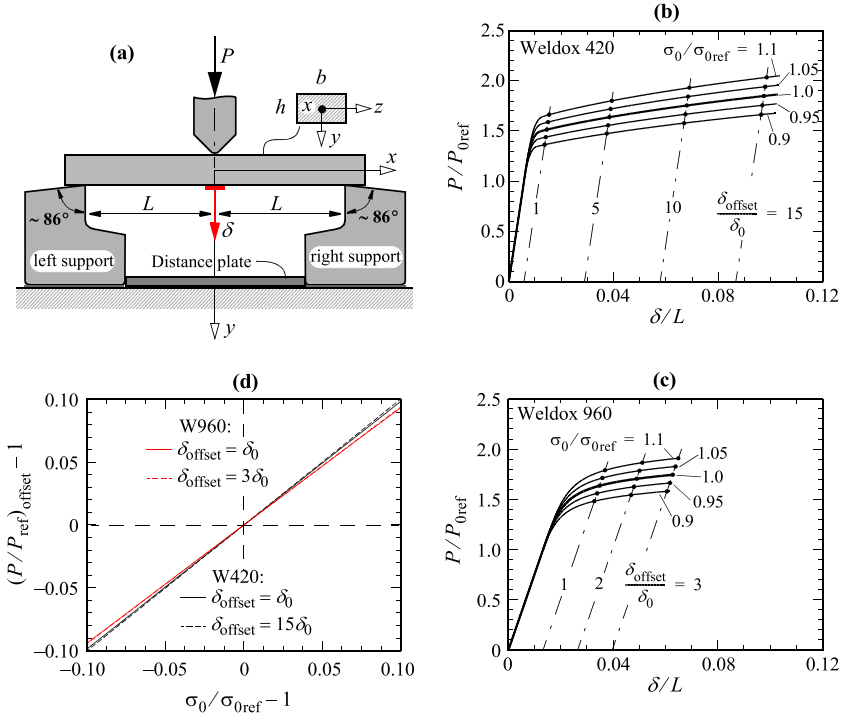

Fig. A1. (a) The set-up for the three-point-bend test; (b) and (c) predictions of load–deflection curves based on a one-dimensional analysis for Weldox 420 and 960, respectively; (d) shows that the relative difference in load ratios evaluated along offset lines is proportional to the relative difference in plastic flow properties.

Table A1
Dimensions of the bend specimens tested as measured after manufacturing.

Test direction:		L1	L2	T2	T2	S1	S2
Weldox 420	b/mm	5.05	5.06	5.06	5.07	5.04	5.04
	h/mm	3.03	3.03	3.03	3.03	3.02	3.03
Weldox 960	b/mm	5.06	5.06	5.05	5.05	5.06	5.06
	h/mm	3.03	3.03	3.02	3.03	3.02	3.02

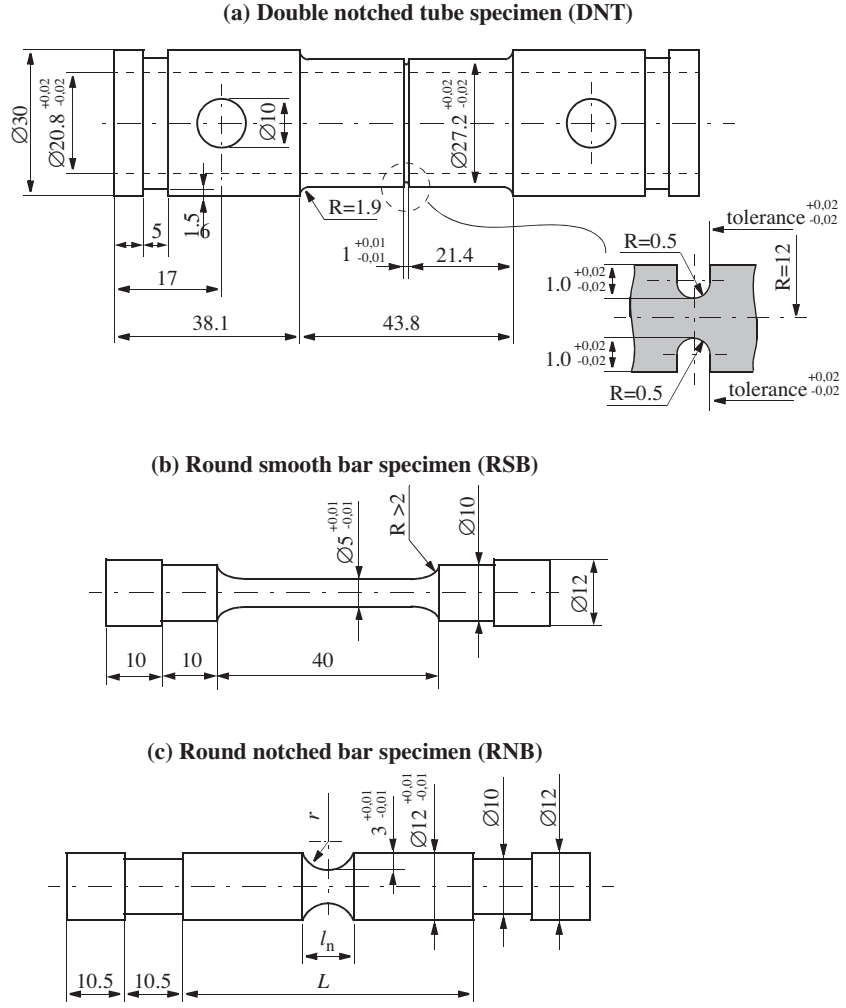

Fig. B1. Detailed drawings of the specimen geometries tested: (a) DNT, double notched tube specimen, (b) RSB, round smooth bar specimen, and (c) RNB, round notched bar specimen.

middle principal stress and located in the plane spanned by the directions of maximum (σ_I) and minimum (σ_{III}) principal stresses, cf. Rudnicki and Rice (1975) and Perrin and Leblond (1993). The normal direction to such a plane can qualitatively be assessed by use of the approximate analysis for the stresses averaged over the notch ligament in Section 3.3. Hence, the Cartesian basis introduced in Fig. 3, will be employed here as depicted in Fig. 12(c).

From the analysis presented in Section 3.3 and based on Eqs. (16) and (17), it is straight forward to express the direction of σ_I by $\mathbf{n}_I = [\mathbf{e}_1 + \alpha\mathbf{e}_2]/\sqrt{1+\alpha^2}$ for all load ratios, with $0 \leqslant \alpha \leqslant 1$ being a dimensionless function of κ and μ ($\alpha = 1$ for $k_T = 0$, and $\alpha = 0$ for $k_T = 1$, see Section 3.3). For the fracture surface shown in Fig. 12(a), $k_T = 0.38$ and hence σ_{III} is defined by (17.2) and its direction may be expressed as $\mathbf{n}_{III} = [-\alpha\mathbf{e}_1 + \mathbf{e}_2]/\sqrt{1+\alpha^2}$. Thus, the normal direction of a presumed plane of plastic localization would be located in the plane spanned by the basis vectors $\mathbf{e}_1$ and $\mathbf{e}_2$, which qualitatively agrees with the orientation of the fracture plane observed in Fig. 12(a). By contrast, for the fracture surface shown in Fig. 12(c), belonging to $k_T = 0.78, \sigma_{III}$ is instead defined by (17.3) and is oriented in the direction $\mathbf{n}_{III} = \mathbf{e}_3$. In this case the normal direction of a presumed plane of plastic localization would instead be located in the plane spanned by the normal vectors $\mathbf{n}_I$ and $\mathbf{e}_3$. Qualitatively, this also agrees with the fracture plane orientation seen in Fig. 12(c). Finally, the fracture shown in Fig. 12(b) is connected to a loading ratio slightly below where axisymmetric condition prevails, and as can be noted, the orientation of the fracture planes seem to be a mixture of those observed in Figs. 12(a and c).

4.4. Comparison of strain at failure in DNT and RNB tests

A detailed account of the RNB tests are given in Barsoum et al. (2012), and only a brief summary will be given here to facilitate a

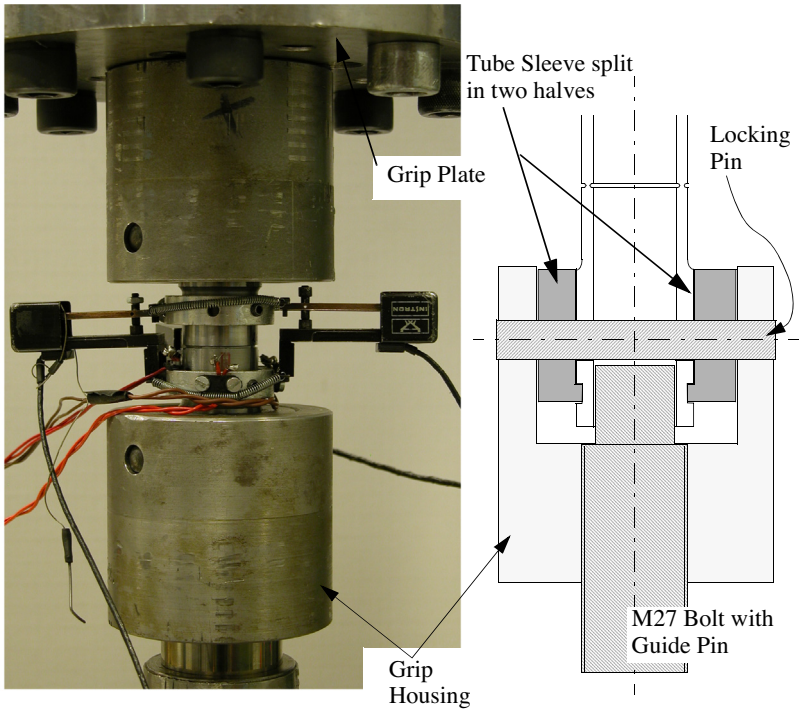

Fig. B2. Fixture used in mounting the DNT specimens into the tension–torsion testing machine.

Table B1
Key results from the DNT tests.

Weldox 420				Weldox 960			
No.	BF	κ	$\bar{\varepsilon}^p_{nf}$	No.	BF	κ	$\bar{\varepsilon}^p_{nf}$
101	–	0	1.397	201	–	0	0.544
102	–	0.090	1.212	202	–	0	0.563
103	–	0.152	0.943	203	–	0.058	0.528
104	–	0.185	1.045	204	–	0.123	0.494
105	–	0.229	1.004	205	–	0.166	0.386
106	–	0.261	0.838	206	–	0.188	0.332
107	–	0.294	0.638	207	–	0.209	0.428
108	–	0.389	0.723	208	–	0.252	0.377
109	–	0.479	0.716	209	–	0.315	0.332
110	–	0.508	0.652	210	–	0.378	0.344
111	–	0.538	0.626	211	–	0.443	0.268
112	1	0.620	0.541	212	1	0.500	0.283
113	2	0.817	0.565	213	–	0.600	0.265
114	3	0.958	0.500	214	2	0.699	0.224
115	4	1.113	0.545	215	3	0.848	0.201
116	5	1.283	0.502	216	4	1.034	0.225
117	6	1.361	0.567	217	5	1.273	0.183
118	7	1.684	0.609	218	6	1.410	0.223
119	8	1.868	0.557	219	7	1.543	0.296
120	9	2.078	0.510	220	8	1.867	0.309
121	10	2.331	0.507	221	9	2.000	0.311
122	11	2.624	0.479	222	10	2.276	0.342
123	12	3.267	0.416	223	11	2.480	0.201
124	13	3.519	0.398	224	12	2.700	0.228
125	14	4.251	0.478	225	13	2.931	0.191
126	15	5.892	0.427	226	14	3.040	0.187
127	16	Inf.	0.354	227	15	3.430	0.215
				228	16	3.47	0.181
				229	17	3.934	0.143
				230	18	4.61	0.153
				231	19	5.73	0.109
				232	20	7.87	0.087
				233	21	Inf.	0.086

Table B2
Key results from the RNB experiments.

Weldox 420				Weldox 960			
No.	$\frac{a}{r}$	T_{ave}	ε^{ρ}_{cf}	No.	$\frac{a}{r}$	T_{ave}	ε^{ρ}_{cf}
101	0.0	0.529	1.572	201	0.0	0.706	1.465
102	0.0	0.630	1.609	202	0.0	0.728	1.438
111	0.2	0.739	1.318	211	0.2	0.833	1.034
112	0.2	0.723	1.241	212	0.2	0.843	1.080
121	0.8	0.930	0.920	213	0.2	0.843	1.078
122	0.8	0.945	1.024	221	0.6	1.004	0.732
131	1.8	1.196	0.599	222	0.6	1.007	0.750
132	1.8	1.196	0.583	223	0.6	1.006	0.742
133	1.8	1.195	0.550	231	1.2	1.231	0.384
141	3.0	1.443	0.351	232	1.2	1.234	0.421
142	3.0	1.438	0.407	233	1.2	1.230	0.365
143	3.0	1.441	0.372	241	2.0	1.483	0.274
151	4.0	1.581	0.258	242	2.0	1.484	0.281
152	4.0	1.581	0.262	243	2.0	1.483	0.268
153	4.0	1.582	0.240	251	3.0	1.697	0.177
				252	3.0	1.702	0.194
				253	3.0	1.699	0.184

comparison of results between the tests carried out on DNT, RSB and RNB specimens, respectively. The equivalent plastic strain at failure (denoted $\bar{\varepsilon}^p_{cf}$), evaluated by FEM analysis at the center point in the neck region in all RNB tests are listed in Table B2 in Appendix B. In Fig. 13, the value of $\bar{\varepsilon}^p_{cf}$ is compared to the average equivalent plastic strain at failure across the neck region evaluated by $2\ln(d_0/d_f)$, as discussed in Section 2.1. Even though the measurements of d_f for practical reasons are somewhat uncertain, the trend is clear: the center value (FEM) and the average value (Exp) come fairly close together at low a/r ratios, whereas at high a/r ratios the center value (FEM) is significantly lower than the average value (Exp). This trend is especially visible in Fig. 13(a) for Weldox

420. The reason for this is that in the presence of a distinct initial notch, the equivalent plastic strain exhibits a strong variation across the notch plane and attains its largest value at the notch surface (not at the center). However, the stress triaxiality is at maximum in the center, where the onset of fracture was observed to occur.

To make a reasonable comparison between the results from the DNT, RSB and RNB tests, center values evaluated by use of finite element analysis at the instant of failure will be used. Results from the three types of specimens are shown in Fig. 14, where $\bar{\varepsilon}^p_{cf}$ is plotted versus T. For the RSB and RNB specimens, an additional set of data is included for each material, that is: $\bar{\varepsilon}^p_{cf}$ plotted versus the average value of triaxiality over the equivalent plastic strain history. Note that this only makes a difference for RSB and the RNB-data with $a/r < 1$, where a marked variation of T was observed during loading due the development of a large geometry change induced by necking, and this was not the case for RNB-tests with a higher ratio of a/r, cf. Barsoum et al. (2012). Recall that in the set of DNT tests, the stress state changes from a *shearing state* to an *axisymmetric state* and back to a *shearing state* as T increases from zero to the maximum value observed in Fig. 14. In the RNB tests an *axisymmetric state* remains valid in the center of the neck region, and there $L = -1$. Thus, it would then be expected that the values of $\bar{\varepsilon}^p_{cf}$ from the two test geometries should coincide at T values where both geometries exhibit an axisymmetric stress state. And indeed, this is the case, as seen for both materials in Fig. 14. This is especially evident if the history average value of T is used to quantify triaxiality in the RSB and RNB tests. Moreover, the sensitivity of the deviatoric stress state on the failure strain seems to diminish at higher values of triaxiality for the medium strength medium hardening steel Weldox 420, as can be observed in Fig. 14(a) by comparing the $\bar{\varepsilon}^p_{cf}$ values from DNT and RNB tests with T larger than about 0.8. However, this is not the case for the high strength low hardening steel Weldox 960, where the deviatoric stress state appears to exert a significant influence $\bar{\varepsilon}^p_{cf}$ even at the highest T values seen in Fig. 14(b). As noted above, the data presented here suggests that the failure strain seems to correlate better with a history average value of T instead of the current value at failure. But, in the tests reported here, only minor deviations from proportional stress paths were present. For highly non-proportional stress histories, a history average value of T may be misleading, which most recently is demonstrated by Benzerga et al. (2012).

5. Conclusions

The experiments on the double notched tube (DNT) specimens presented in Barsoum and Faleskog (2007a) have been extended with a significant amount of new experiments to cover the full range possible down to zero stress triaxiality. Two materials were tested, Weldox 420—a medium strength medium hardening steel and Weldox 960—a high strength low hardening steel. A new and robust procedure for the evaluation of the equivalent plastic strain was proposed and an approximate stress analysis was presented that laid the ground for an unambiguous and qualitatively clear understanding of the experimental outcome. Also, a set of experiments carried out on round notched bar (RNB) specimens, presented in Barsoum et al. (2012), was recapitulated to give a comprehensive and collective overview of the ductile failure characteristics for the two materials tested in the broad triaxiality range: $0 \leqslant T \leqslant 1.6$. The experimental data base will be used in the companion paper (Part II) to explore the predictive capability of the Gurson model extended for shear failure recently proposed by Nahshon and Hutchinson (2008).

The experiments clearly demonstrated that the equivalent plastic strain at failure is not a monotonic function of stress triaxiality, T, in the two materials tested. Even though the stresses and strains were not uniform in the test sections of the specimens, the stress path was close to proportional in the regions were onset of fracture occurred. The non-monotonic behavior observed in failure strain could therefore unambiguously be explained by the differences in the deviatoric stress state between the tests. Specifically, the two materials withstood a higher strain at failure when subjected to axisymmetric stressing than if subjected to shear dominated stressing, if conditions were such that the stress triaxiality otherwise was not changed. Here, the Lode parameter L or the parameter ω, was employed to distinguish between axisymmetric and shear dominated stressing, respectively, i.e., to quantify the deviatoric stress state. The sensitivity to L (or ω) was for both materials most apparent at low values of T. For the high strength low hardening steel Weldox 960 this sensitivity of L on T persisted in the whole range of triaxiality explored, i.e., up to T values well above unity. However, this was not the case for the medium strength medium hardening steel Weldox 420, where the influence of L on T markedly weakened for T values slightly below unity and seemed to diminish for T values above unity.

Acknowledgements

The authors are grateful to M.Sc. H. Öberg for suggesting the use of a bend specimen to examine the degree of anisotropy in plastic flow properties, and also for doing those tests. The authors are also indebted to Prof. J.W. Hutchinson for fruitful discussions.

Appendix A.

Fig. A1(a) shows the experimental setup of a three-point-bend test used to investigate the relative difference between the plastic flow properties in the three directions: L (rolling direction), T (transverse rolling direction in-plane), S (short transverse, direction of thickness). The specimen, a uniform prismatic bar with rectangular cross section $(b \times h)$ with a testing span of $2L$, was mounted in a servo-hydraulic testing machine on two supports. Each support has an acute angle of about 86°, so that the distance between the contact points during a test was essentially constant. The supports were kept in place by a distance plate, which ensured that the span $2L$ was the same in all tests and equal to 26 mm. The deflection of the bar was measured by a LVDT displacement transducer on the opposite side of the loading point. Load was applied in displacement control at a rate of 0.01 mm/s, and the force and displacement data records were sampled with a frequency of 6.3 Hz. The relative error of the measuring devices, i.e., the LVDT and the load cell, were less than 0.001 in the plastic domain. The specimens were manufactured by electrical discharge machining, which exerts a minimal influence on the material next to the machined surface. To eliminate a possible influence of small variations in specimen dimensions on the relative differences in plastic flow properties in the three directions, the central portion $(|x| \leqslant L/2)$ of each specimen was carefully measured prior to testing and the results are listed in Table A1. The accuracy of these measurements was within ± 5 μm.

A variation in plastic flow properties will influence the P–δ curve and this influence can be ascertained by a rather simple one-dimensional analysis, as briefly outlined next. The longitudinal strain at a generic point of the cross-section of the bar may be expressed as y/R_c throughout the loading, where R_c is the radius of curvature of the neutral surface. By assuming uniaxial conditions (neglecting the shear stress), the corresponding longitudinal stress can be phrased as $\sigma(\varepsilon) = \sigma_0 f(\varepsilon)$, where σ_0 represents the initial yield stress and $f(\varepsilon)$ is a non-linear function of strain representing the uniaxial stress–strain response. If the non-dimensional variables $\psi = 2y/h$ $(|\psi| \leqslant 1)$ and $\rho = 2R_c/h$ are introduced, and

the uniaxial response for the two Weldox materials described in Eq. (3) is adopted, f may be recast into a function of ψ as

$$f(\psi)=\begin{cases}\psi/(\rho\varepsilon_0) & |\psi|\leqslant\rho\varepsilon_0\\ \mathrm{sgn}(\psi) & \rho\varepsilon_0<|\psi|\leqslant\rho(\varepsilon_s+\varepsilon_N)\\ \mathrm{sgn}(\psi)\cdot[(|\psi|-\rho\varepsilon_s)/(\rho\varepsilon_N)]^N & \rho(\varepsilon_s+\varepsilon_N)\leqslant|\psi|\leqslant 1\end{cases} \tag{A.1}$$

Moreover, the distribution of the bending moment in the bar can be expressed as

$$P(L-x)/2=2\int_0^{h/2}y\sigma(\varepsilon)b\mathrm{d}y \tag{A.2}$$

By use of the non-dimensional variables established above and introducing $\xi=x/L$ and $\overline{P}=3PL/(\sigma_0bh^2)$, Eq. (A.2) can be written as

$$\overline{P}(1-\xi)=F(\rho^{-1})\quad\text{with } F(\rho^{-1})=3\int_0^1\psi f(\psi)\mathrm{d}\psi \tag{A.3}$$

Note, that the onset of plastic yielding occurs when $\overline{P}=1$ at $\xi=0$ for $\rho=1/\varepsilon_0$. Let v be the deflection of the bar in the y-direction. For the present purpose it is justified to neglect effects of large rotations in the expression for curvature, hence the relation $\mathrm{d}^2v/\mathrm{d}x^2=h\rho/2$. The deflection, δ, can then be calculated for a certain value of $\overline{P}$ in the following way: (i) solve Eq. (A.3) numerically for the normalized curvature ρ in the whole domain $0\leqslant\xi\leqslant1$; (ii) integrate $\mathrm{d}^2v/\mathrm{d}x^2$ numerically with the boundary conditions $\mathrm{d}v/\mathrm{d}x=0$ at $\xi=0$ and $v=0$ at $\xi=1$. Evaluation of v at $\xi=0$ may then be expressed as

$$\delta=L\cdot\frac{L}{h}\cdot\Delta\ (\overline{P};\ \text{Mat.param.})$$

Here, Δ is a non-dimensional function of the normalized load $\overline{P}$, and the material parameters in (A.1).

In Fig. A1(b) and (c), the influence of a variation of the initial yield stress on the load–deflection curve for the two materials Weldox 420 and 960 is illustrated. All curves are normalized by $P_{0\mathrm{ref}}=\sigma_{0\mathrm{ref}}bh^2/(3L)$, where $\sigma_{0\mathrm{ref}}$ is taken as the respective material value (σ_0) listed in Table 1. The curves represent a variation of the initial yield stress in the range $0.9\leqslant\sigma_0/\sigma_{0\mathrm{ref}}\leqslant1.1$. All curves were terminated when the maximum longitudinal strain reached a value of 0.10. As can be observed from Fig. A1(b) and (c), an appropriate range for the evaluation of differences in plastic flow properties may be defined by the offset lines as $P/k_0+\delta^1_{\mathrm{offset}}\leqslant\delta\leqslant P/k_0+\delta^2_{\mathrm{offset}}$, where k_0 being the initial (elastic) slope and $\delta^i_{\mathrm{offset}}/\delta_0=\eta_i$, with $\delta_0=P_{0\mathrm{ref}}/k_0$. Suitable values of η_i for the two materials are suggested by the figures. In Fig. A1(d), the relative difference between the load–deflection curves and the reference curve along several offset lines are plotted versus the relative difference in the initial yield stress. Note that there is virtually a one-to-one correspondence between the relative differences in the load–deflection curves and the initial yield stress, respectively. Thus, by carrying out tests with bar specimens oriented in the three perpendicular directions, the experimental setup discussed here seems to be a viable and practical way to detect a possible anisotropy in the plastic properties.

Appendix B.

The dimensions with the key manufacturing tolerances of the specimens used to characterize the uniaxial stress–strain response (RSB) and the ductility (DNT and RNB) of the material are displayed in Fig. B1. The inner and outer notch in a DNT specimen was machine-finished with the same lathe tool, which specifically was produced for this purpose. Hence, the shape of the inner and outer notch was expected to be identical. The ligament thickness between the notches was not measured after the manufacturing, and was expected to be within the tolerances. However, in the specimens tested, the axial alignment of the inner and outer notch, respectively, was checked to be within tolerances after the manufacturing. It should be pointed out that a small variation of the ligament thickness between the notches, essentially only affect the load levels and not the development of plastic strains to a critical level, whereas a strong variation in the axial alignment of the notches also seriously would affect the plastic response in the notch region.

Fig. B2 shows the fixture used to mount the DNT specimen into the MTS tension–torsion testing machine. As a first step, when a series of DNT tests were to be conducted, the two grip housings were bolted to the testing machine. The lower grip housing was bolted to the piston of the machine and the upper grip housing to a grip plate. The grip plate was mounted to the load cell of the machine by eight bolts, and this was done as an integral part of the alignment of the fixture. The alignment was accomplished by first mounting a stiffer dummy specimen to the lower and upper grip housings (the dummy specimen had the same inner diameter as the DNT specimen, an outer diameter of 30 mm and was lacking notches). The dummy specimen was provided with three strain gauges placed at equal distance along the circumference to measure the longitudinal strain. Fastening of the grip plate to the load cell was then done in such a way that the three strain gauges did not deviate from each other when an axial load was applied. Once the fixture was aligned, the dummy specimen was removed and the DNT specimen to be tested was mounted to the grip housings in the following way. A tube sleeve with an inwards flange, split in two halves, was first attached to each one of the ends of the specimen, such that a tight connection was established between each flange and the matching circumferential slot of the specimen. Each end of the specimen, with a tube sleeve attached, was then inserted into a grip housing, positioned by the guide pin, and mounted to it by a locking pin, see Fig. B2. Transfer of loading from the MTS machine to a DNT specimen was effectuated as follows: the axial force was transmitted from the grip housing via the locking pin to the tube sleeve and then finally to the specimen via the circumferential slots; the torque was transmitted from the grip housing directly to the specimen via the looking pin. It should be pointed out that a good alignment was crucial in the tests dominated by tension, i.e., for κ values larger than about unity. Therefore, in tests with $\kappa\geqslant0.6$, specimens were equipped with three strain gauges equidistantly placed along the circumference, to facilitate measurements of the longitudinal strain. These measurements were then used to quantify deviations in alignment, see Barsoum and Faleskog (2007a). For practical purposes, the deviation from alignment was observed to be small in all specimens tested.

The key results from all tests performed within the experimental program are listed for the DNT specimens in Table B1 and for the RNB specimens in Table B2. In Table B1, the four columns from left to right contains: specimen number; old specimen number for tests already presented in Barsoum and Faleskog (2007a), referred to as BF; load ratio κ; the overall equivalent plastic strain at failure directly evaluated from test data by Eq. (9). In Table B2, the four columns from left to right contains: specimen number; notch ratio; stress triaxiality averaged over the load history; the equivalent plastic strain in the center of the specimen at failure evaluated by FEM.

References

ABAQUS, 2010. User's Manual Version 6.10, Dassault Systems.
Bao, Y.B., Wierzbicki, T., 2004. On fracture locus in the equivalent strain and stress triaxiality space. International Journal of Mechanical Sciences 46, 81–98.

Barsoum, I., Faleskog, J., 2007a. Rupture mechanisms in combined tension and shear—experiments. International Journal of Solids and Structures 44, 1768–1786.

Barsoum, I., Faleskog, J., 2007b. Rupture mechanisms in combined tension and shear—micromechanics. International Journal of Solids and Structures 44, 5481–5498.

Barsoum, I., Faleskog, J., 2011. Micromechanical analysis on the influence of the Lode parameter on void growth and coalescence. International Journal of Solids and Structures 48, 925–938.

Barsoum, I., Faleskog, J., Pingle, S., 2012. The effect of stress state on ductility in the moderate stress triaxiality regime of medium and high strength steels. International Journal of Mechanical Sciences 65, 203–212.

Benzerga, A.A., Surovik, D., Keralavarma, S.M., 2012. On the path-dependence of the fracture locus in ductile materials – analysis. International Journal of Plasticity 37, 157–170.

Dunand, M., Mohr, D., 2011. Optimized butterfly specimen for the fracture testing of sheet materials under combined normal and shear loading. Engineering Fracture Mechanics 78, 2919–2934.

Gao, X.S., Faleskog, J., Shih, C.F., 1998. Cell model for nonlinear fracture analysis – II. Fracture-process calibration and verification. International Journal of Fracture 89, 375–398.

Gao, X.S., Zhang, G.H., Roe, C., 2010. A study on the effect of the stress state on ductile fracture. International Journal of Damage Mechanics 19, 75–94.

Gao, X.S., Zhang, T.T., Hayden, M., Roe, C., 2009. Effects of the stress state on plasticity and ductile failure of an aluminum 5083 alloy. International Journal of Plasticity 25, 2366–2382.

Graham, S.M., Zhang, T.T., Gao, X.S., Hayden, M., 2012. Development of a combined tension-torsion experiment for calibration of ductile fracture models under conditions of low triaxiality. International Journal of Mechanical Sciences 54, 172–181.

Gruben, G., Fagerholt, E., Hopperstad, O.S., Borvik, T., 2011. Fracture characteristics of a cold-rolled dual-phase steel. European Journal of Mechanics A – Solids 30, 204–218.

Haltom, S.S., Kyriakides, S., Ravi-Chandar, K., 2013. Ductile failure under combined shear and tension. International Journal of Solids and Structures 50, 1507–1522.

McClintock, F.A., 1971. Plasticity aspects of fracture. In: Liebowitz, H. (Ed.), Fracture III, An Advanced Treatise. Academic Press, New York, pp. 47–225.

Mohr, D., Henn, S., 2007. Calibration of stress-triaxiality dependent crack formation criteria: a new hybrid experimental–numerical method. Experimental Mechanics 47, 805–820.

Nahshon, K., Hutchinson, J.W., 2008. Modification of the Gurson Model for shear failure. European Journal of Mechanics A – Solids 27, 1–17.

Narström, T., 2013. Private communication.

Perrin, G., Leblond, J.B., 1993. Rudnicki and Rice's analysis of strain localization revisited. Journal of Applied Mechanics 60, 842–846.

Rudnicki, J.W., Rice, J.R., 1975. Conditions for the localization of deformation in pressure-sensitive dilatant materials. Journal of the Mechanics and Physics of Solids 23, 371–394.

Tvergaard, V., 2008. Shear deformation of voids with contact modelled by internal pressure. International Journal of Mechanical Sciences 50, 1459–1465.

Tvergaard, V., 2009. Behaviour of voids in a shear field. International Journal of Fracture 158, 41–49.

Tvergaard, V., Nielsen, K.L., 2010. Relations between a micro-mechanical model and a damage model for ductile failure in shear. Journal of the Mechanics and Physics of Solids 58, 1243–1252.

Xue, Z., Faleskog, J., Hutchinson, J.W., 2013. Tension-torsion fracture experiments—Part II: simulations with the extended Gurson model and a fracture criterion based on plastic strain. International Journal of Solids and Structures 50, 4258–4269.

Xue, Z., Pontin, M.G., Zok, F.W., Hutchinson, J.W., 2010. Calibration procedures for a computational model of ductile fracture. Engineering Fracture Mechanics 77, 492–509.